Additive manufactured AlSi10Mg samples using Selective Laser Melting (SLM): Microstructure, high cycle fatigue, and fracture behaviour

Erhard Brandl[a*], Ulrike Heckenberger[a], Vitus Holzinger[a], Damien Buchbinder[b]

a EADS Innovation Works, Metallic Technologies & Surface Engineering, D-81663 Munich, Germany, erhard.brandl@eads.net, ulrike.heckenberger@eads.net, vitus.holzinger@eads.net

* Corresponding author: T +49 (0)89 607 22107, F +49 (0)89 607 25408

b Fraunhofer Institute for Lasertechnology (ILT), Steinbachstr. 15, D-52074 Aachen, Germany, damien.buchbinder@ilt.fraunhofer.de

ABSTRACT

In order to produce serial parts via additive layer manufacturing, the fatigue performance can be a critical attribute. In this paper, the microstructure, high cycle fatigue (HCF), and fracture behaviour of additive manufactured AlSi10Mg samples are investigated. The samples were manufactured by a particular powder-bed process called Selective Laser Melting (SLM) and machined afterwards. 91 samples were manufactured without (30°C) and with heating (300°C) of the building platform and in different directions (0°, 45°, 90°). Samples were tested in the peak-hardened (T6) and as-built condition. The Wöhler curves were interpolated by a Weibull distribution. The results were analysed statistically by design of experiments, correlation analysis, and mariginal means plots. The investigations show that the post heat treatment has the most considerable effect and the building direction has the least considerable effect on the fatigue resistance. The fatigue resistance of the samples, however, is high in comparison to the standard DIN EN 1706. The combination of 300°C platform heating and peak-hardening is a valuable approach to increase the fatigue resistance and neutralize the differences in fatigue life for the 0°, 45°, and 90° directions.

Keywords: A. Non-ferrous metals and alloys; E. Fatigue; G. Scanning electron microscopy

1 Introduction

Building up components in a layer-by-layer fashion is mostly referred to as rapid prototyping (RP), rapid manufacturing (RM), additive manufacturing (AM), or additive layer manufacturing (ALM). All of those technologies share the layer-additive approach: A three-dimensional CAD model is sliced into thin layers. With the slice file, the particular ALM process builds the physical part layer by layer. Today, this approach enables the building of complex geometries from polymers, metals, and ceramics within a few hours. According to [1], the ALM technology includes four process routes: powder-bed, powder-feed, wire-feed, and other processes. Depending on the authors and topic of publication, the number of process routes is often reduced to two or three. For example, in [2] the process routes of ALM contain only powder-feed and wire-feed processes.

In a powder-bed process, a laser or electron beam traces the part's pattern on a thin powder layer. The building platform then moves down by the thickness of one layer (typically below 150 µm) and a new powder layer is deposited onto the previous one. The beam traces the pattern of the second layer, and the melted areas of the two layers are joined. The process continues until the part is finished. The process is illustrated as a schematic drawing in Figure 1.

Figure 1 Schematic drawing of powder-bed additive layer manufacturing [1]

Manufacturing components by powder-bed processes offers the highest geometrical flexibility and accuracy in comparison with the other ALM process routes. The construction of small metallic parts with complex shapes (e.g. internal cooling channels) and high resolution is feasible only using this process route. Nowadays, several laser- and electron beam based processes are commercially available [3]. In the present paper, samples from the casting alloy AlSi10Mg are manufactured using a laser based process called Selective Laser Melting (SLM).

In comparison to the static tensile performance, the fatigue performance of additive manufactured components is mostly disregarded. The growing market demand on additive

manufactured serial parts (“Rapid manufacturing” instead of “Rapid Prototyping”) [3, 4] increasingly implies fatigue investigations, especially for dynamically loaded applications.

2 Experimental details

2.1 Powder-bed process (SLM - Selective Laser Melting)

The particular SLM process is based on a Trumpf TrumaForm LF130 powder-bed machine (Figure 2).

Figure 2 Powder-bed machine used (Trumpf)

The circular building platform has a diameter of Ø 130 mm and can be heated up to 500°C. The powder is melted by a diode pumped Nd:YAG laser with 250 W maximum beam power. Further details of this particular SLM process and investigations on aluminium alloys can be found elsewhere [5-11].

For the experiments of this paper, the following parameters were applied:

- Laser beam power of 250 W
- Laser beam diameter of Ø 0.2 mm
- Layer thickness of 50 µm
- Laser scanning speed of 500 mm/s
- Laser scanline spacing of 0.15 mm
- Argon gas shielding

The platform temperature was chosen to 30°C for three batches and 300°C for six batches. A heating of the platform reduces residual stresses and distortion of the components built [9].

2.2 Aluminium alloy AlSi10Mg

The aluminium alloy used for this study is AlSi10Mg. This is a a widely used alloy for aluminium castings [12]. The hypoeutectic alloy is near the eutectic composition (12.5 % Si) which is responsible for the excellent casting properties [12, 13]. Figure 3 shows the phase diagram of Al-Si.

Figure 3 Phase diagram of Aluminium-Silicon after [13]

Minor additions of magnesium (0.3 - 0.5 % are most beneficial) allow hardenability by natural or artifical ageing [13]. Table 1 shows the chemical composition of the AlSi10Mg alloy used. The compositions of all batches measured were within this specification.

Table 1 Chemical composition of the alloy AlSi10Mg [13]

The material is used as powder. The particle size of the AlSi10Mg powder is in the range of 25 - 45 µm.

2.3 Mechanical characterization

High cycle fatigue (HCF) samples (Figure 4) with stress concentration factor $K_t \approx 1$ were built with material allowance (1 mm), machined according to ASTM E466 [14], and tested according to EN 6072 [15] at room temperature on a Microtron 654 (Rumul) resonance tester.

Figure 4 High cycle fatigue sample

A test frequency of approximately 108 Hz and a stress ratio of $R = \sigma_{min}/\sigma_{max} = 0.1$ were used. The HCF tests were terminated at $3 \cdot 10^7$ cycles.

The static tensile tests were performed according to DIN ISO EN 6892 [16] at the company Festo AG & Co KG (Germany). Samples A4x20 were used according to DIN 50125 [17]. The static tensile properties are published elsewhere in detail [9, 18] and are therefore not repeated in this paper.

2.4 Microscopic characterization

Polished cross-sections were etched for 15 s using 0.5 % HF in water according to [19] and also evaluated according to [19]. Light microscopy pictures were taken with a Polyvar microscope (Reichert-Jung). The fracture surfaces were analyzed by LEO 1430 scanning electron microscope.

2.5 Statistical analysis

The Woehler curves were interpolated by the Weibull distribution according to equation (1) [20]. The Weibull constant

- c_1 refers to 45% of the fatigue limit (MPa) and represents the limit $\sigma_a = 0.45 \cdot \sigma_{max} = c_1$ for N

$\rightarrow \infty$,

- c_2 refers to 45% of the static tensile strength (MPa) and represents the limit $\sigma_a = 0.45 \cdot \sigma_{max} = c_2$ for $N \rightarrow 0$,
- c_3 and c_4 (dimensionless) influence the slope and shape of the Wöhler curve between the two asymptotes. The fatigue resistance σ_{max} increases with an increasing Weibull constant c_3 and decreases with an increasing c_4.

By means of equations (2) and (3), the Weibull distribution can be written in dependence of the maximum stress σ_{max} shown in equation (4).

Stress amplitude $$\sigma_a = c_1 + \frac{c_2 - c_1}{e^{\left[\frac{\lg(N)}{c_3}\right]^{c_4}}} \quad (1)$$

Stress ratio $$R = 0.1 = \frac{\sigma_{min}}{\sigma_{max}} \quad (2)$$

Stress amplitude $$\sigma_a = \frac{\sigma_{max} - \sigma_{min}}{2} = \frac{\sigma_{max} - 0.1 \cdot \sigma_{max}}{2} = 0.45 \cdot \sigma_{max} \quad (3)$$

Maximum stress $$\sigma_{max} = \frac{2}{0.9} \cdot \left(c_1 + \frac{c_2 - c_1}{e^{\left[\frac{\lg(N)}{c_3}\right]^{c_4}}}\right) = \frac{1}{0.45} \cdot \left(c_1 + \frac{c_2 - c_1}{e^{\left[\frac{\lg(N)}{c_3}\right]^{c_4}}}\right) \quad (4)$$

Statistical analysis was perfomed by correlation analysis and marginal means plots. For that purpose, the design of experiments software DOE PRO XL (SigmaZone) and Excel 2003 (Microsoft) was used. The influence of the process parameters, building direction, and post heat treatment on the Weibull constants ($c_1 - c_4$) and the correlation between these constants were determined.

2.6 Post built-up heat treatment

Some samples were peak-hardened (PH) to T6 condition:

- Solution heat treatment for 6 h at 525°C
- Room temperature water quench
- Artificial aging for 7 h at 165°C

The particular peak-hardening (chosen from experience) usually results in maximum tensile and yield strengths with adequate elongation. Peak-hardening was carried out before final

machining of the samples to remove the surface layer that was influenced from the treatment (e.g. residual stresses, distortions, contaminations).

2.7 Sample manufacturing

In total, 91 HCF samples were built. Table 2 gives an overview of the batches and the different conditions.

Table 2 Details of the high cycle fatigue batches

The samples were built in three different directions (Figure 5). The longitudinal axis of the samples is parallel to the x-y plane at 0° and perpendicular to the x-y plane, i.e. parallel to the z-axis, at 90°.

Figure 5 Samples (static tensile) built in different directions: (a) 0°, (b) 45°, (c) 90° after [9]

Besides the direction, the samples were built at different platform temperatures (30°C, 300°C) and post heat treated differently (as-built, T6).

3 Results

3.1 Microstructure

To determine the porosity, polished and unetched micrographs are investigated. Porosity is visible in all batches with pores generally below 300 µm (Figure 6, Figure 7). The density for every batch was measured by means of a test sample and shows a density above 99%.

Figure 6 Typical micrograph (polished, unetched) of batch #12 (30°C/45°/Peak-hardened); plane is perpendicular to the longitudinal axis of the sample

Figure 7 Typical micrograph (polished, unetched) of batch #17 (300°C/45°/as-built); plane is perpendicular to the longitudinal axis of the sample

According to the phase diagram (Figure 3), the microstructure (Figure 8 - Figure 12) is characterized by the size and arrangement of the

- α-Al matrix (bright phase),
- eutectic Si-particles (dark phase).

Besides, a minor amount of the phases Mg_2Si, $Al_9Fe_2Si_2$, $Al_8Si_9Mg_3Fe$ can appear according to [19].

Figure 8 Typical microstructure of batch #10 (30°C/0°/Peak-hardened); plane is perpendicular to the longitudinal axis of the sample

Figure 9 Typical microstructure of batch #11 before peak-hardening (30°C/90°/as-built); plane is perpendicular to the longitudinal axis of the sample; (a) macro view, (b) micro view

Figure 10 Typical microstructure of batch #11 (30°C/90°/Peak-hardened); plane is perpendicular to the longitudinal axis of the sample

Figure 11 Typical microstructure of a batch #13 (300°C/0°/as-built); plane is perpendicular to the longitudinal axis of the sample

Figure 12 Typical microstructure of batch #14 (300°C/0°/Peak-hardened); plane is perpendicular to the longitudinal axis of the sample

Regarding the microstructure (Figure 8 - Figure 12), the following observations can be made:

- The as-built microstructure (Figure 9, Figure 11) is characterized by cellular dendrites of α-Al and the interdentritic Si-particles. The laser traces and resulting heat affected zones with coarser dendrites are visible resulting in an inhomogenous microstructure. Similar observations are published in [8].
- After peak-hardening, the eutectic Si-particles have coarsened and formed to a globular shape. The microstructure is homogenous and there is no significant microstructural difference between 0°, 45°, and 90° samples apparent. Dendrites, laser traces, and heat affected zones are not visible any more.

3.2 High cycle fatigue (HCF) properties

Figure 13 − Figure 15 show the the fatigue resistance (σ_{max}), i.e. $\sigma_{max} = \sigma_{min}/ 0.1$, versus number of cycles. The maximum stresses σ_{max} applied were determined with respect to the yield strengths of the batches, which are published elsewhere [9, 18]. The 30°C/0°/Peak-hardened batch (#10) shows the highest and the as-built batches (#13, #15, #17) show the lowest fatigue resistance. The scatter of each batch is low compared to different ALM material [1, 21]. According to DIN EN 1706 [22], the fatigue resistance to rotating bending of EN AC-AlSi10Mg(Fe) at $5 \cdot 10^7$ cycles is $\sigma_{max} = 60 - 90$ MPa. All batches tested exceed this range (mostly by far). It should be noted that this comparison is even conservative: The fatigue resistance at completely reversed stressing (R = -1) tends to be higher at rotating bending than at tension-compression and the latter one tends to be higher than at tension-tension (R = 0.1), at

which these samples were tested.

Figure 13 shows the fatigue resistance of the samples built at 30°C platform temperature. It can be observed for the

- 30°C/Peak-hardened samples: The fatigue resistance is higher in 0° than in 45° and 90° direction.

Figure 13 Fatigue resistance and Weibull distribution (50% probability of failure) of batches that are built at 30°C platform temperature; the samples #10.1, #10.4 are used for the fracture surface analysis

Figure 14 shows the fatigue resistance of the samples built at 300°C platform temperature. It can be observed for the

- 300°C samples: Peak-hardening increases the fatigue resistance considerably.
- 300°C samples: The fatigue resistance is comparable in 0°, 45°, and 90° direction.

Figure 14 Fatigue resistance and Weibull distribution (50% probability of failure) of batches that are built at 300°C platform temperature; the samples #13.4, #13.9, #14.2, #14.7, #16.3, and #16.7 are used for the fracture surface analysis

Figure 15 shows the fatigue resistance of the peak-hardened samples. It can be observed for the

- Peak-hardened samples: the fatigue resistance in 45° and 90° direction is significantly higher when built at 300°C than at 30°C.

Figure 15 Fatigue resistance and Weibull distribution (50% probability of failure) of batches that are peak-hardened (PH)

3.3 Statistical analysis

Table 3 shows the design of experiments (DoE) matrix consisting of a full-factorial experiment design with two levels (low, high) and three factors (platform temperature A, building direction B, and post heat treatment C). The batches #12, #17, and #18 (building direction of 45°) could not be included in the statistical analysis as the design has only two levels, but the batches #1 and #5 (static tensile and high cycle fatigue properties published in [18]) were included.

Table 3 Design of experiments matrix (full-factorial, 2 levels, 3 factors); static tensile and high cycle fatigue properties of batches #1 and #5 are published in [18]

Table 4 shows the correlation and probability analysis of the Weibull constants. The correlation tests determine if there is a linear relationship between two variables that do not logically depend on one another. The higher the absolute value of correlation (≤ 1), the higher is the correlation between the two variables. The lower the p(robability)-value, the more significant is this correlation. Mostly for $p < 0.05$, the effect is regarded as statistically significant.

Table 4 Correlation and probability analysis of the Weibull constants $c_1 - c_4$

The following important results can be obtained from Table 4:

- The fatigue limit (i.e. c_1) and tensile strength (i.e. c_2) significantly correlate with each other (absolute value of correlation: 0.747, p-value < 0.05)
- The Weibull constants c_3 and c_4 do not significantly correlate with each other or with c_1 and c_2 (p-value >> 0.05)

Figure 16 – Figure 19 show the marginal means plots of the platform temperature, building direction, and post heat treatment with respect to the Weibull constants $c_1 - c_4$. The marginal means plots are a graphical representation of the impact of the factors on the Weibull constants. The larger the difference between the "Low" (effect level: 0) and the "High" (effect level: 1), the longer is the line and the larger is the larger impact on the Weibull constant.

Figure 16 Marginal means plot of platform temperature, building direction, and post heat treatment with respect to the Weibull coefficient c_1 (45% of the fatigue limit)
Figure 17 Marginal means plot of platform temperature, building direction, and post heat treatment with respect to the Weibull coefficient c_2 (45% of the tensile strength)
Figure 18 Marginal means plot of platform temperature, building direction, and post heat treatment with respect to the Weibull coefficient c_3
Figure 19 Marginal means plot of platform temperature, building direction, and post heat treatment with respect to the Weibull coefficient c_4

The following results can be obtained from the marginal means plots:

- The post heat treatment has the most considerable effect on the Weibull constants c_1 (i.e. fatigue limit), c_2 (i.e. tensile strength), and c_4. The Weibull constants c_1 and c_2 increase

(consequently the fatigue resistance is increased) and c_4 increases (consequently the fatigue resistance is decreased) when the samples are peak-hardened.

- The platform temperature and post heat treatment have a similar and considerable effect on the Weibull constant c_3. The constant c_3 decreases (consequently the fatigue resistance is decreased) when the platform is preheated to 300°C and when the samples are peak-hardened.
- The building direction has a relatively small influence on the Weibull constants c_1 (i.e. fatigue limit), c_3, and c_4 compared to the platform temperature and post heat treatment.

3.4 Fracture surfaces

Figure 20 - Figure 23 show scanning electron microscope pictures of the crack initiation site (breakthrough crack) and area of forced fracture for selected samples. For a batch, one sample with a high stress and low number of cycles, and one sample with a lower stress and high number of cycles, were analyzed: samples #10.10 and #10.4 (see Figure 13), samples #13.4 and #13.9 (see Figure 14), samples #14.2 and #14.7 (see Figure 14), samples #16.7 and #16.3 (see Figure 14).

Figure 20 Typical fracture surfaces of two samples from batch #10 (30°C/0°/Peak-hardened): (a) crack initiation site and (b) area of forced fracture of sample #10.10; (c) crack initiation site and (d) area of forced fracture of sample #10.4

Figure 21 Typical fracture surfaces of two samples of batch #13 (300°C/0°/as-built): (a) crack initiation site and (b) area of forced fracture of sample #13.4; (c) crack initiation site and (d) area of forced fracture of sample #13.9

Figure 22 Typical fracture surfaces of two samples of batch #14 (300°C/0°/Peak-hardened): (a) crack initiation site and (b) area of forced fracture of sample #14.2; (c) crack initiation site and (d) area of forced fracture of sample #14.7

Figure 23 Typical fracture surfaces of two samples of batch #16 (300°C/90°/Peak-hardened): (a) crack initiation site and (b) area of forced fracture of sample #16.7; (c) crack initiation site and (d) area of forced fracture of sample #16.3

The following oberservations can be made from Figure 20 - Figure 23:

- The breakthrough cracks always start from the surface or subsurface (pores, non melted spots). This was also observed at the samples not shown in this paper.
- The peak-hardened samples show dimples in the area of forced fracture in comparison to the

as-built samples (Figure 21b,d and Figure 22b,d), which suggests a ductile fracture behaviour [23].

- Each peak-hardened sample shows a similar (ductile) forced fracture behaviour (Figure 20, Figure 22, Figure 23), which is not significantly dependent on the platform temperature (30°C, 300°C) or building direction (0°, 90°).

4 Discussion

Imperfections, such as porosity or shrinkage cavities, greatly influences the fatigue life of cast components as shown in numerous investigations, e.g. [24-29]. Regarding ALM, the imperfections are to some extent different to the ones of castings. It is commonly observed in ALM material that defects, i.e. pores or regions of non-melted powder (lack of fusion), primarily form between layers and are aligned parallel to them [30-34]. The defects reduce the effective load-bearing area perpendicular to the layers (z-direction) and cause stress concentration (notch effect), resulting in reduction of static and dynamic strength in z-direction [35]. A reduced strength in z-direction was even taken into account in standardisation activities [36]. According to [37-39], porosity has the most detrimental effect on fatigue properties of castings, especially when pore size and amount exceed certain values. When either pore size or amount of porosity is reduced below a certain critical level, the next mechanism in the hierarchy becomes operational and dominates fatigue behaviour [39], e.g. microstructural features [40]. This contributes to an explanation of why peak-hardening (PH) has the most considerable impact on the fatigue resistance, i.e. Weibull constants $c_1 - c_4$ (see Figure 16 − Figure 19). As shown in Figure 8 - Figure 12, the microstructure was homogenized, microstructural differences (e.g. heat-affected zones) were eliminated, the interdentritic eutectic Si-particles have become spheroidal (like cast iron with nodular/spheroidal graphite [41]). This reduced crack initiation and/or propagation, which in total increased the fatigue resistance. Peak-hardening also seems to increase ductility as the area of forced fracture showed dimples (Figure 22b,d) in contrast to the as-built samples (Figure 21b,d). The elongation of failure in

the static tensile tests [18], however, did not significantly increase or decrease at the 300°C samples after peak-hardening, but increased considerably at the 30°C samples.

A further observation was that the fatigue resistance of the 300°C samples is comparable in the 0°, 45°, and 90° direction, in contrast to the 30°C samples. The building direction, however, showed the least considerable impact on the Weibull constants compared to the other factors (see Figure 16 − Figure 19). It can be imagined that the 300°C platform heating leads to fewer imperfections (e.g. non-melted spots), as the laser beam can heat up to higher temperatures and the cooling rate and distortion is reduced. Furthermore, the 300°C heating leads to fewer residual stresses [9], which might also contribute to a higher fatigue resistance. Fewer imperfections can also be the reason for a higher fatigue resistance in the 45° and 90° direction at 300°C platform temperature than at 30°C. A positive effect of fewer imperfections becomes especially evident in the 45° and 90° direction. In the 0° direction, the effect cannot be seen as clearly as imperfections are aligned parallel to the load (smallest notch-effect). As already mentioned above, additive manufactured components generally show the highest static and dynamic strength in the 0° direction for that reason [1, 36]. The presented fatigue results verify this common tendency as the 30°C samples showed the highest dynamic strength in the 0° direction (Figure 13). It was also figured out that static tensile strength and fatigue limit significantly correlate with each other (Table 4).

Besides, it was observed that the breakthrough cracks always started from imperfections (pores, non-melted spots) at the surface or subsurface. Crack initiation from the surface or subsurface is generally expected due to the stress conditions and localized plastic deformation induced by surface discontinuities [23, 29, 42]. The imperfections, however, can turn into a surface-notch after final machining and even promote crack initiation. The process (scanning strategy of the laser beam, flow of inert gas, powder deposition etc.) must therefore be improved to avoid such imperfections as they are constantly present throughout the batches. This could also explain why the scattering is relatively low compared to other additive manufactured HCF samples

showing higher densities [1, 21]. Although the SLM microstructure is different to castings, a similarity with respect to imperfections is present: surface or subsurface porosity is also the most important defect affecting the fatigue life as it is the most likely site for crack initiation [28, 29].

5 Conclusions

Microstructure, high cycle fatigue properties, and fracture surfaces of selective laser melted AlSi10Mg samples were investigated. The following main results were obtained:

- The as-built microstructure is characterized by cellular dendrites of α-Al and interdentritic Si-particles.
- After peak hardening to T6, the microstructure is homogenous, i.e. dendrites, laser traces, and heat affected zones dissolved, and Si-particles formed to a globular shape. A significant microstructural difference between 0°, 45°, and 90° is not apparent any more.
- The area of forced-fracture of the peak-hardened samples showed pronounced dimples in contrast to the as-built samples.
- The fatigue limit (i.e. c_1) and static tensile strength (i.e. c_2) significantly correlate with each other.
- In contrast to samples built at 300°C, samples built at 30°C show a higher fatigue resistance in 0° than in 45° and 90° direction.
- Peak-hardening has the most considerable and building direction has the least significant impact on the fatigue resistance.
- After peak-hardening, the fatigue resistance of samples built at 300°C increased considerably and was still comparable in 0°, 45°, and 90° direction.
- The breakthrough cracks always start from the surface or subsurface (pores, non-melted spots).

From the results, the following main conclusions can be drawn:

- The combination of 300°C platform heating and peak-hardening is a valuable approach to

increase the fatigue resistance (and static tensile strength) and neutralize the differences in fatigue life for the 0°, 45°, and 90° directions.

- The process parameters (scanning strategy of the laser beam, powder deposition etc.) must be improved to increase the current density (≥ 99%) and avoid imperfections. Despite the porosity and imperfections observed, the fatigue resistance of the samples is very high compared to the standard DIN EN 1706 [22].

Acknowledgment

The authors would like to thank the german government (BMBF) for the funding of the project "AluGenerativ" (01RI0639A-D) and would like to thank the project executor DLR, project partner Fraunhofer ILT, BMW Group, Daimler AG, Festo AG & Co. KG, Eckagranules GmbH, ZfW gGmbH and inno-shape GmbH. The activities at EADS Innovation Works were especially supported by Achim Schoberth, Frank Palm, Birgit Vetter, Christian Plander, and Dr. Claudio Dalle Donne.

References

[1] Brandl E. Microstructural and mechanical properties of additive manufactured titanium (Ti-6Al-4V) using wire: Evaluation with respect to additive processes using powder and aerospace material specifications. Aachen: Shaker Verlag; 2010.
[2] Baufeld B, van der Biest O., Gault R. Additive Manufacturing of Ti-6Al-4V components by shaped metal deposition: microstructure and mechanical properties. Mat Des. 2010;31:106-11.
[3] Wohlers TT. Wohlers report 2010. Fort Collins, Colorado: Wohlers Associates; 2010.
[4] Santos EC, Shiomi M, Osakada K, Laoui T. Rapid manufacturing of metal components by laser forming. International Journal of Machine Tools and Manufacture. 2006;46:1459-68.
[5] Buchbinder D, Meiners W, Wissenbach K, Müller-Lohmeier K, Brandl E. Rapid manufacturing of aluminium parts for serial production via selective laser melting (SLM). Aluminium Alloys. Aachen 2008. p. 2394-400.
[6] Meiners W. Direktes selektives Laser Sintern einkomponentiger metallischer Werkstoffe. Aachen: Shaker Verlag; 1999.
[7] Over C. Generative Fertigung von Bauteilen aus Werkzeugstahl X38CrMoV5-1 und Titan TiAl6V4 mit "Selective Laser Melting". Aachen: Shaker Verlag; 2003.
[8] Zhang D. Entwicklung des Selective Laser Melting für Aluminiumwerkstoffe. Aachen: Shaker Verlag; 2004.
[9] Buchbinder D, Meiners W, Wissenbach K, Müller-Lohmeier K, Brandl E, Skrynecki N. Rapid manufacturing of aluminium parts for serial production via selective laser melting (SLM). 4 International Conference on Rapid Manufacturing. Loughborough: University 2009.
[10] Buchbinder D, Meiners W, Wissenbach K, Müller-Lohmeier K, Brandl E. Rapid Manufacturing von Aluminiumbauteilen für die Serienproduktion durch Selective Laser Melting (SLM). Euro-uRapid. Frankfurt (Germany): Fraunhofer Allianz; 2007.

[11] Buchbinder D, Schleifenbaum H, Heidrich S, Meiners W, Bültmann J. High Power Selective Laser Melting (HP SLM) of Aluminium Parts. Physics Procedia. 2011;12:271-8.
[12] Vojtech D, Serak J, Ekrt O. Improving the casting properties of high-strength aluminium alloys. Materiali in Tehnologije. 2004;38:99-102.
[13] Kammer C. Aluminium Taschenbuch Band 1. Düsseldorf: Aluminium Verlag; 2009.
[14] ASTM International. Standard Practice for Conducting Constant Amplitude Axial Fatigue Tests of Metallic Materials. ASTM E 466-07: ASTM International; 2007.
[15] Standard. Aerospace series - Metallic materials - Test methods - Constant amplitude fatigue testing. DIN EN 6072:20102010.
[16] Standard. Metallic materials - Tensile testing - Part 1: Method of test at room temperature. DIN EN ISO 6892-1:20092009.
[17] Deutsche Norm. Test pieces for tensile testing of metallic materials. DIN 50125: Deutsches Institut für Normung; 2004.
[18] TIB Hannover: D. Buchbinder. Generative Fertigung von Aluminiumbauteilen für die Serienproduktion, Förderkennzeichen: 01RI0639A-D. Aachen: Fraunhofer Institute for Laser Technology ILT; 2010.
[19] Kovacheva R. Metallographic investigation of Al-Si-Mg and Al-Si-Cu alloys. Praktische Metallographie. 1993;30:68-81.
[20] Luftfahrttechnisches Handbuch - Handbuch Struktur Berechnung (HSB): IASB; 2003.
[21] Baufeld B, Brandl E, van der Biest O. Wire based additive layer manufacturing: comparison of microstructure and mechanical properties of Ti-6Al-4V components fabricated by laser-beam deposition and shaped metal deposition. J Mat Proc Techn. 2011;211:1146-58.
[22] Deutsche Norm. Aluminium und Aluminiumlegierungen - Gussstücke - Chemische Zusammensetzung und mechanische Eigenschaften. DIN EN 1706: Deutsches Institut für Normung; 2010.
[23] Grosch J. Schadenskunde im Maschinenbau. Renningen: expert Verlag; 2004.
[24] Zhang B, Sung PK, Poirier DR, Chen W. Effects of Strontium Modification and Hydrogen Content on the Fatigue Behavior of A356.2 Cast Aluminum Alloy AFS Transactions. 2000;108:383-9.
[25] Sonsino CM, Ziese J. Fatigue strength and applications of cast aluminium alloys with different degrees of porosity. International Journal of Fatigue. 1993;15:75-84.
[26] Pedersen JAØK. Fatigue Properties of an A356 (AlSi7Mg) Aluminium Alloy for Automotive Applications - Fatigue Life Prediction. International Congress & Exposition 1994.
[27] Major JF. Porosity control and fatigue behavior in A356-T61 aluminum alloy. AFS Transactions. 1997;105:901-6.
[28] Ammar HR, Samuel AM, Samuel FH. Effect of casting imperfections on the fatigue life of 319-F and A356-T6 Al-Si casting alloys. Materials Science and Engineering: A. 2008;473:65-75.
[29] Ammar HR, Samuel AM, Samuel FH. Porosity and the fatigue behavior of hypoeutectic and hypereutectic aluminum-silicon casting alloys. International Journal of Fatigue. 2008;30:1024-35.
[30] Kobryn PA, Semiatin SL. Mechanical properties of laser-deposited Ti-6Al-4V. JOM. 2006.
[31] Stucker B, Janaki Ram G. Layer-Based Additive Manufacturing Technologies. Materials Processing Handbook: CRC Press; 2007. p. 1-32.
[32] Thijs L, Verhaeghe F, Craeghs T, Humbeeck JV, Kruth J-P. A study of the microstructural evolution during selective laser melting of Ti-6Al-4V. Acta Materialia. 2010;58:3303-12.

[33] Murr LE, Gaytan SM, Ceylan A, Martinez E, Martinez JL, Hernandez DH, et al. Characterization of titanium aluminide alloy components fabricated by additive manufacturing using electron beam melting. Acta Materialia. 2009;58:1887-94.
[34] Bos MJ, Amsterdam E, Kool GA. High Cycle Fatigue of Laser Beam Deposited Ti-6Al-4V and Inconel 718. ICAF 2009, Bridging the Gap between Theory and Operational Practice: Springer Netherlands; 2009. p. 1261-74.
[35] Kelbassa I. Qualifizieren des Laserstrahl-Auftragschweißens von BLISKs aus Nickel- und Titanbasislegierungen [Dissertation]: RWTH Aachen; 2006.
[36] SAE Aerospace. Titanium alloy direct deposited products 6Al - 4V annealed. AMS 4999A: Aerospace Material Specification; 2008.
[37] Couper MJ, Neeson AE, Griffiths JR. Casting defects and the fatigue behaviour of an aluminium casting alloy. 1990;13:213-27.
[38] Wang QG, Apelian D, Lados DA. Fatigue behavior of A356-T6 aluminum cast alloys. Part I. Effect of casting defects. Journal of Light Metals. 2001;1:73-84.
[39] Lados DA, Apelian D. Fatigue crack growth characteristics in cast Al-Si-Mg alloys: Part I. Effect of processing conditions and microstructure. Mat Sci Eng A. 2004;385:200-11.
[40] Wang QG, Apelian D, Lados DA. Fatigue behavior of A356-T6 aluminum cast alloys. Part II. Effect of microstructural constituents. Journal of Light Metals. 2001;1:85-97.
[41] Radzikowska JM. Metallography and Microstructures of Cast Iron. Metallography and Microstructures. 2nd edition ed. Ohio (USA): ASM International; 2004. p. 565-87.
[42] Qian G, Hong Y, Zhou C. Investigation of high cycle and Very-High-Cycle Fatigue behaviors for a structural steel with smooth and notched specimens. Engineering Failure Analysis. 2011;17:1517-25.

Figures

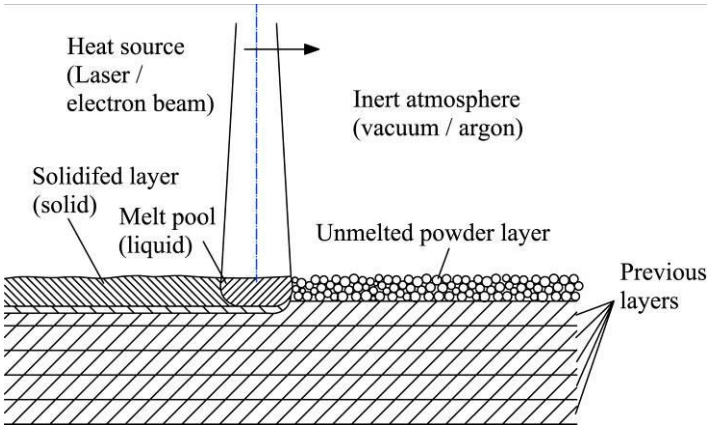

Figure 1 Schematic drawing of powder-bed additive layer manufacturing [1]

Figure 2 Powder-bed machine used (Trumpf)

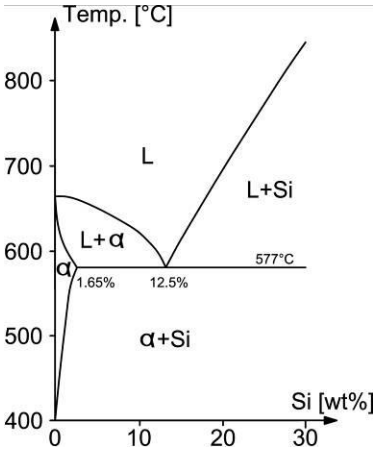

Figure 3 Phase diagram of Aluminium-Silicon after [13]

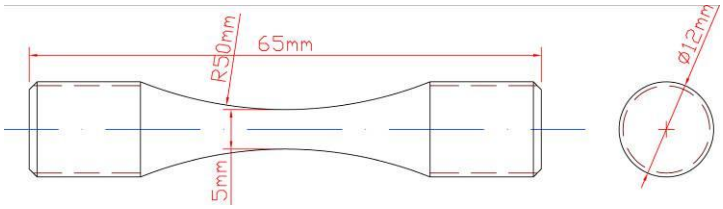

Figure 4 High cycle fatigue sample

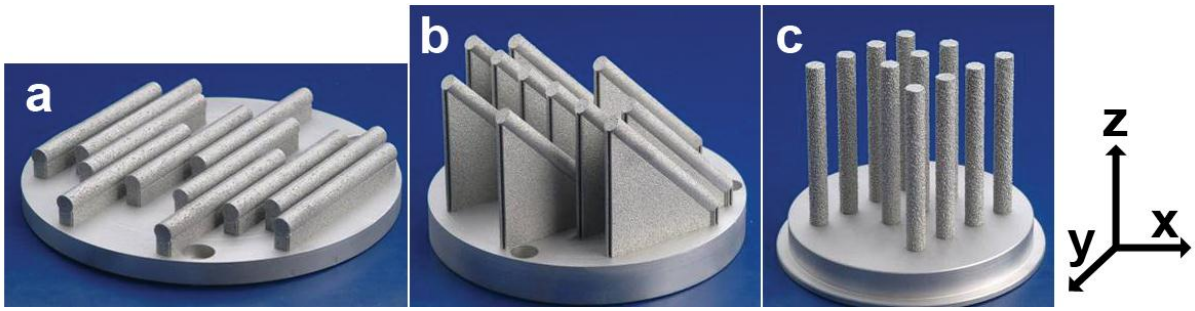

Figure 5 Samples (static tensile) built in different directions: (a) 0°, (b) 45°, (c) 90° after [9]

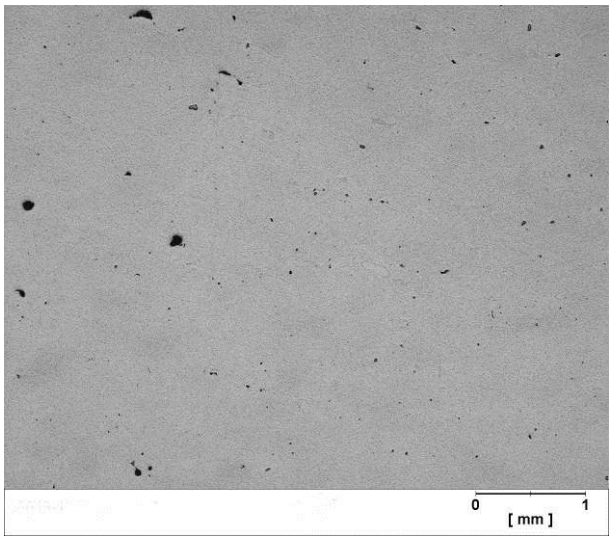

Figure 6 Typical micrograph (polished, unetched) of batch #12 (30°C/45°/Peak-hardened); plane is perpendicular to the longitudinal axis of the sample

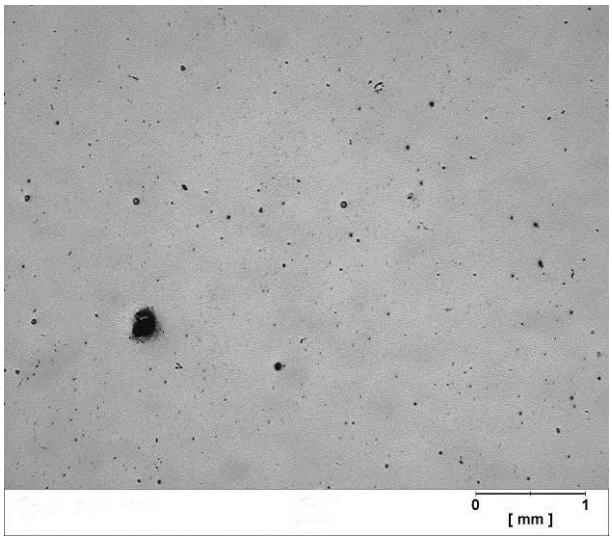

Figure 7 Typical micrograph (polished, unetched) of batch #17 (300°C/45°/as-built); plane is perpendicular to the longitudinal axis of the sample

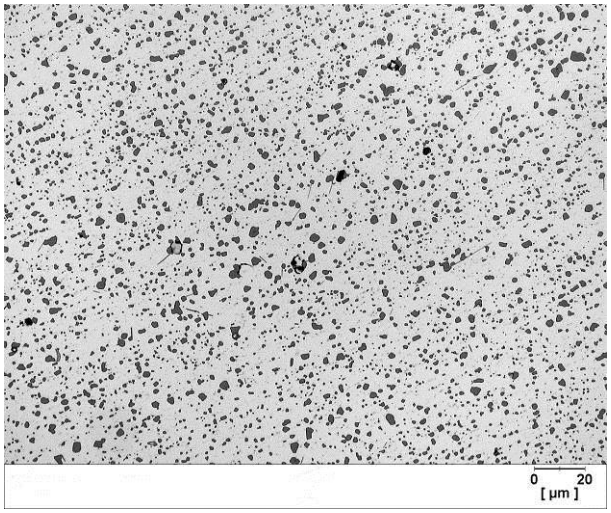

Figure 8 Typical microstructure of batch #10 (30°C/0°/Peak-hardened); plane is perpendicular to the longitudinal axis of the sample

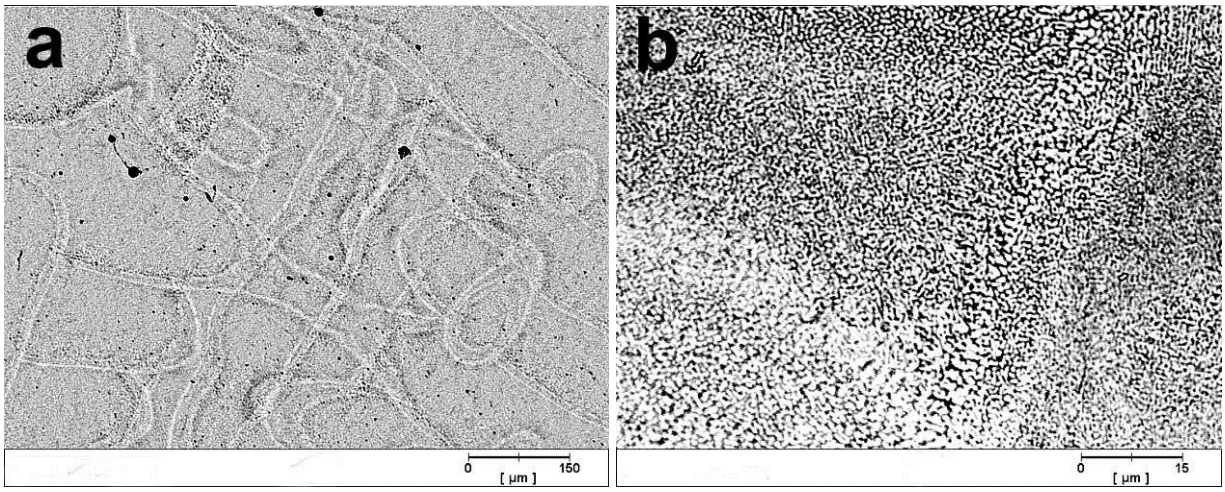

Figure 9 Typical microstructure of batch #11 before peak-hardening (30°C/90°/as-built); plane is perpendicular to the longitudinal axis of the sample; (a) macro view, (b) micro view

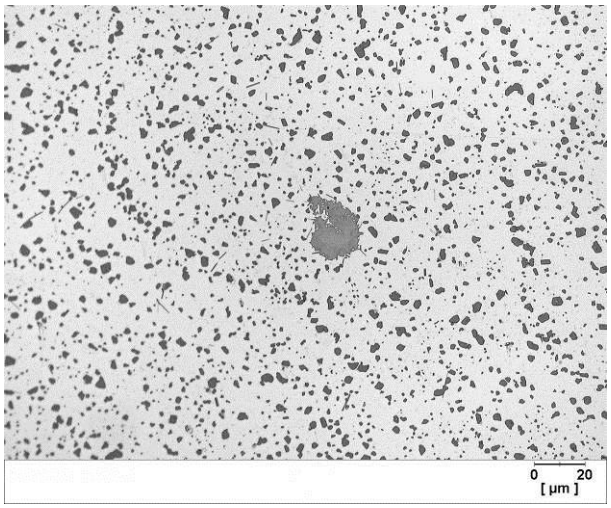

Figure 10 Typical microstructure of batch #11 (30°C/90°/Peak-hardened); plane is perpendicular to the longitudinal axis of the sample

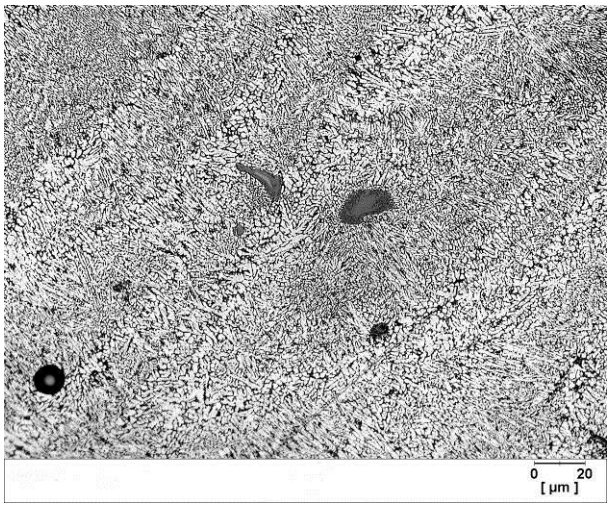

Figure 11 Typical microstructure of a batch #13 (300°C/0°/as-built); plane is perpendicular to the longitudinal axis of the sample

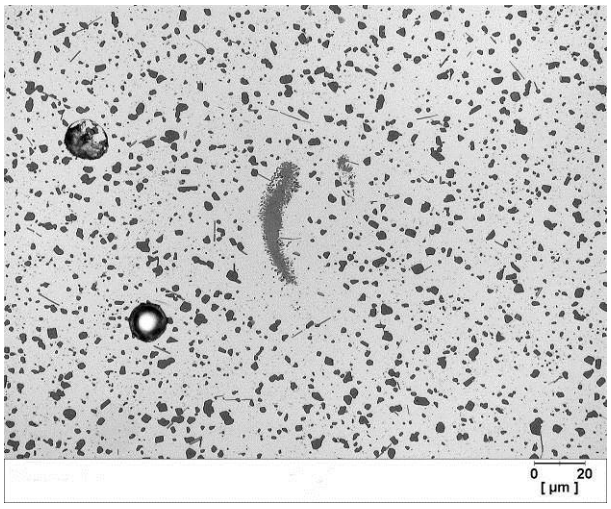

Figure 12 Typical microstructure of batch #14 (300°C/0°/Peak-hardened); plane is perpendicular to the longitudinal axis of the sample

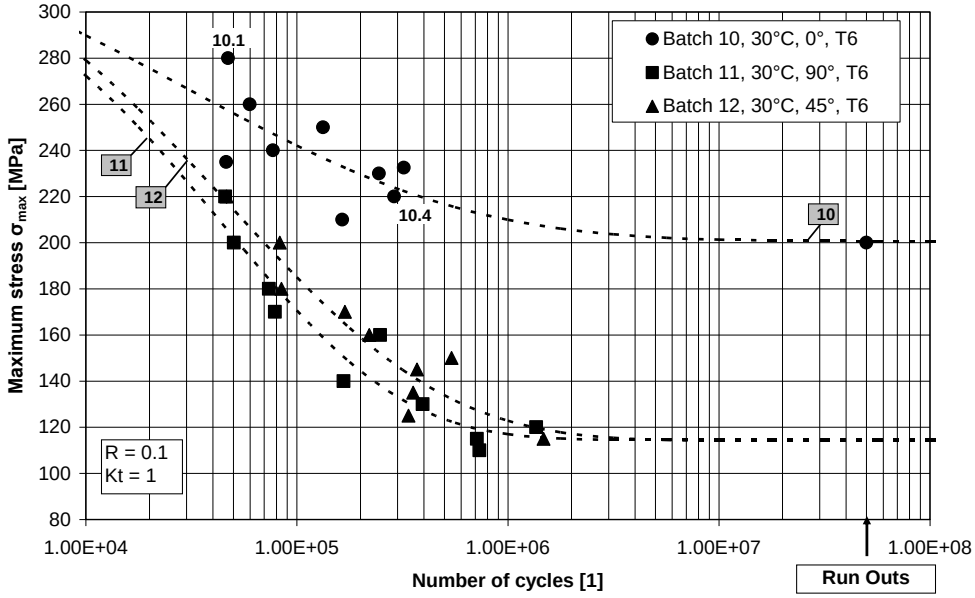

Figure 13 Fatigue resistance and Weibull distribution (50% probability of failure) of batches that are built at 30°C platform temperature; the samples #10.1, #10.4 are used for the fracture surface analysis

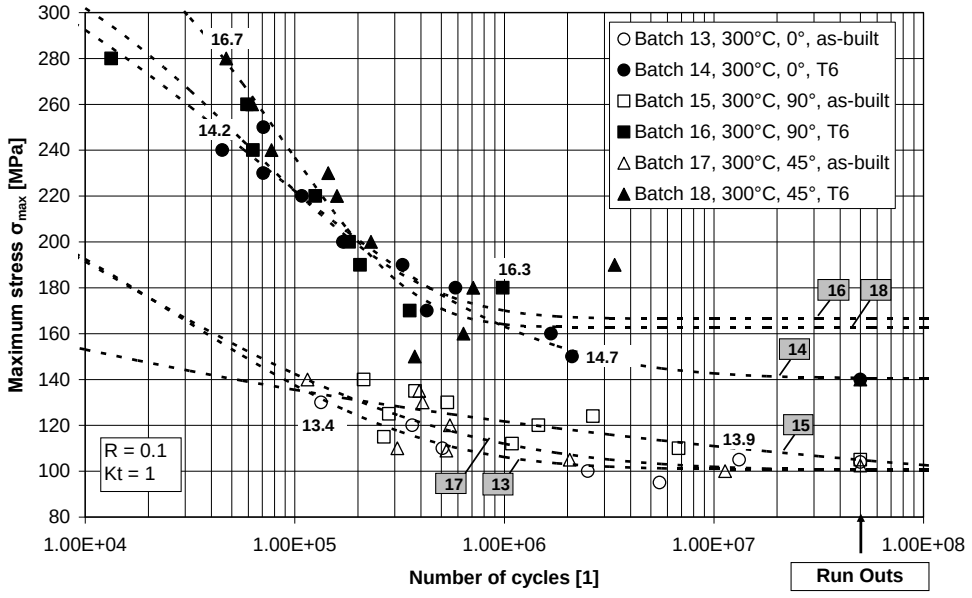

Figure 14 Fatigue resistance and Weibull distribution (50% probability of failure) of batches that are built at 300°C platform temperature; the samples #13.4, #13.9, #14.2, #14.7, #16.3, and #16.7 are used for the fracture surface analysis

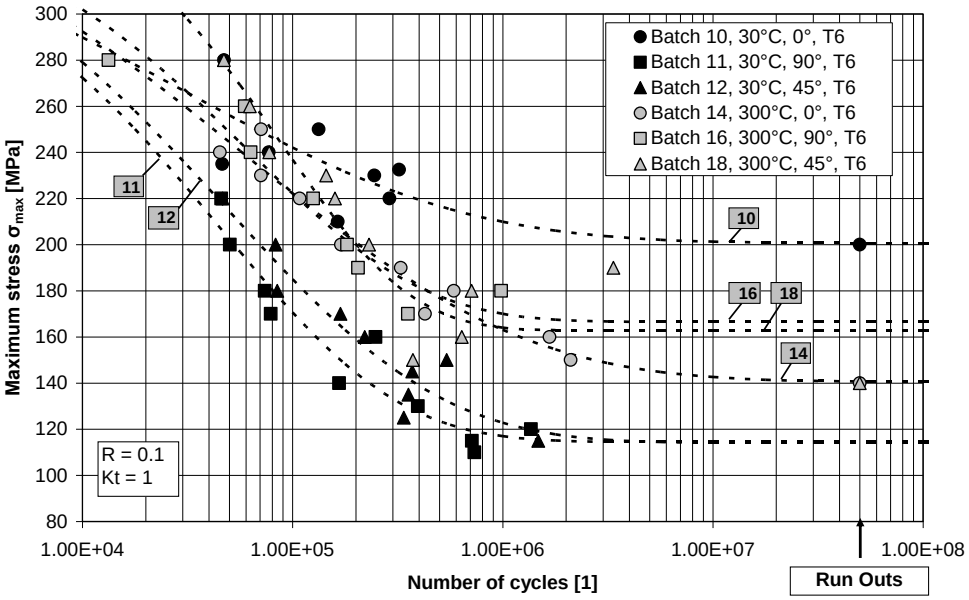

Figure 15 Fatigue resistance and Weibull distribution (50% probability of failure) of batches that are peak-hardened (PH)

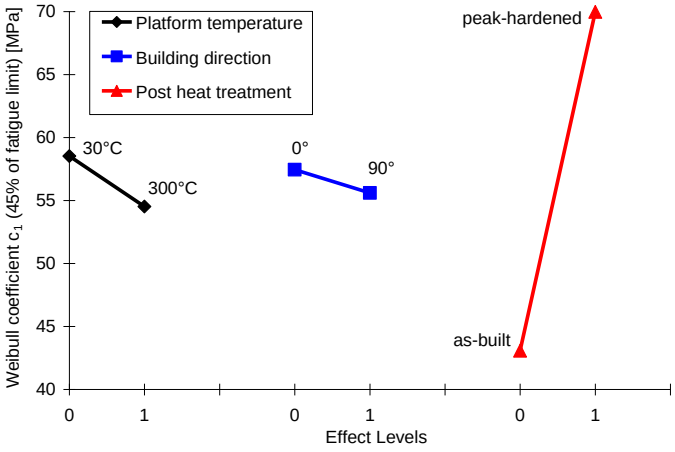

Figure 16 Marginal means plot of platform temperature, building direction, and post heat treatment with respect to the Weibull coefficient c_1 (45% of the fatigue limit)

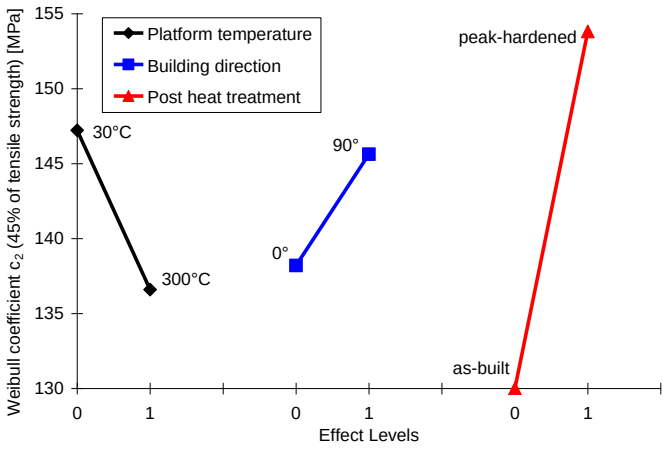

Figure 17 Marginal means plot of platform temperature, building direction, and post heat treatment with respect to the Weibull coefficient c_2 (45% of the tensile strength)

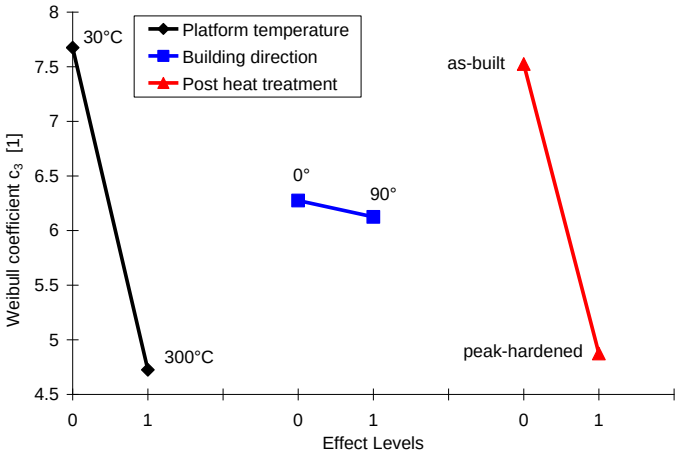

Figure 18 Marginal means plot of platform temperature, building direction, and post heat treatment with respect to the Weibull coefficient c_3

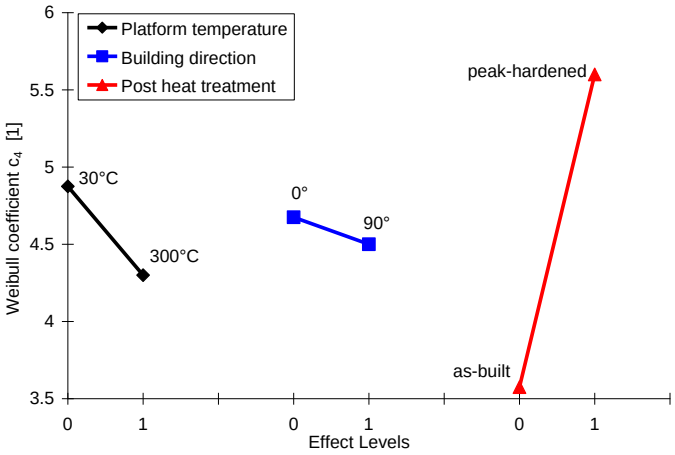

Figure 19 Marginal means plot of platform temperature, building direction, and post heat treatment with respect to the Weibull coefficient c_4

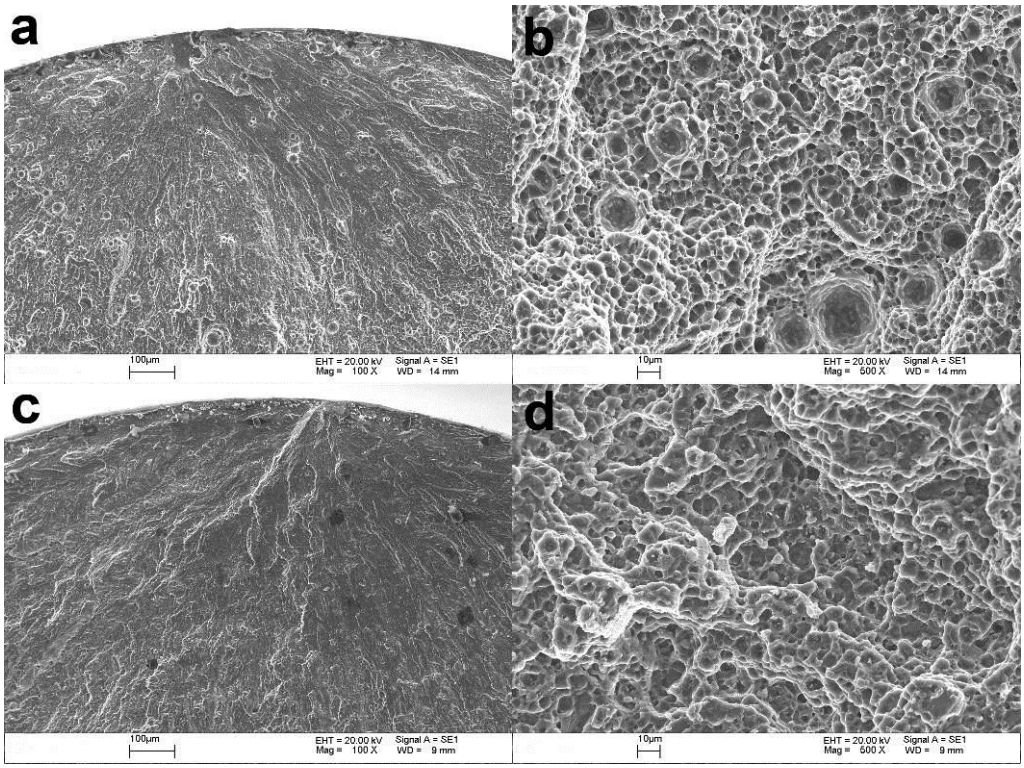

Figure 20 Typical fracture surfaces of two samples from batch #10 (30°C/0°/Peak-hardened): (a) crack initiation site and (b) area of forced fracture of sample #10.10; (c) crack initiation site and (d) area of forced fracture of sample #10.4

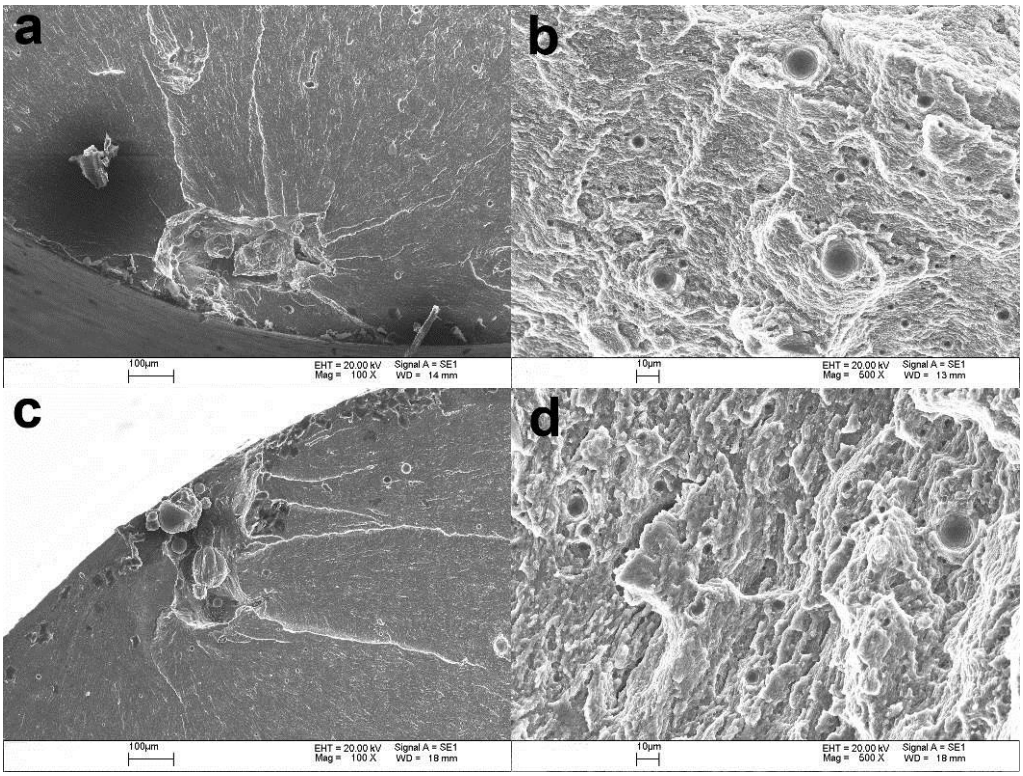

Figure 21 Typical fracture surfaces of two samples of batch #13 (300°C/0°/as-built): (a) crack initiation site and (b) area of forced fracture of sample #13.4; (c) crack initiation site and (d) area of forced fracture of sample #13.9

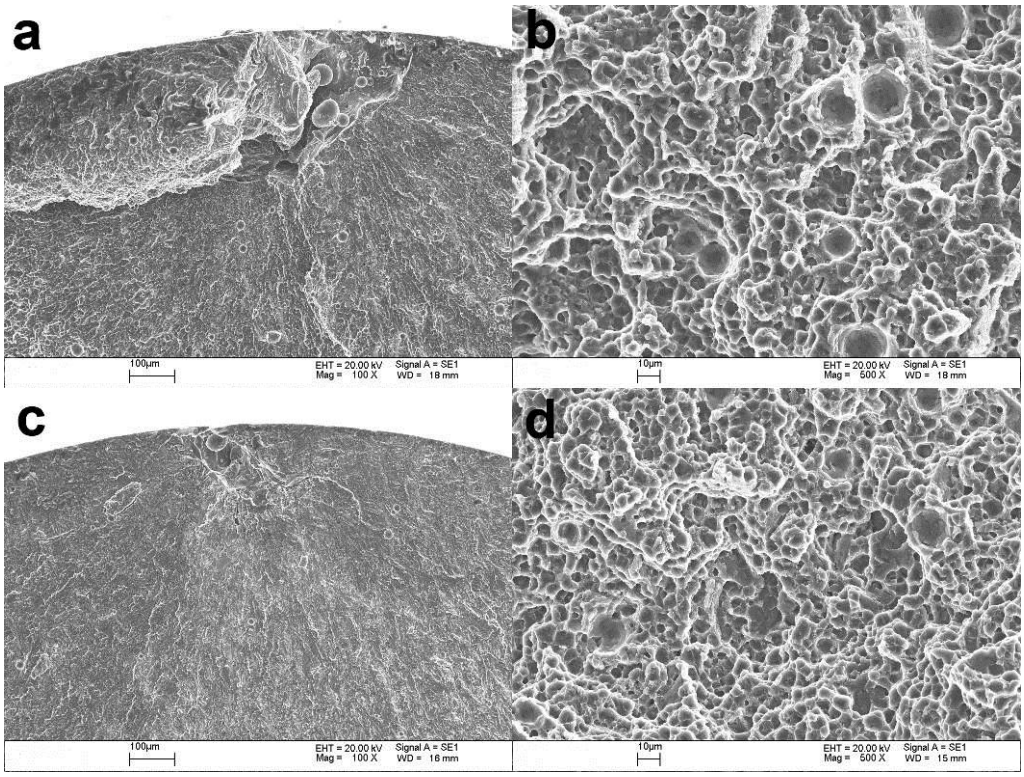

Figure 22 Typical fracture surfaces of two samples of batch #14 (300°C/0°/Peak-hardened): (a) crack initiation site and (b) area of forced fracture of sample #14.2; (c) crack initiation site and (d) area of forced fracture of sample #14.7

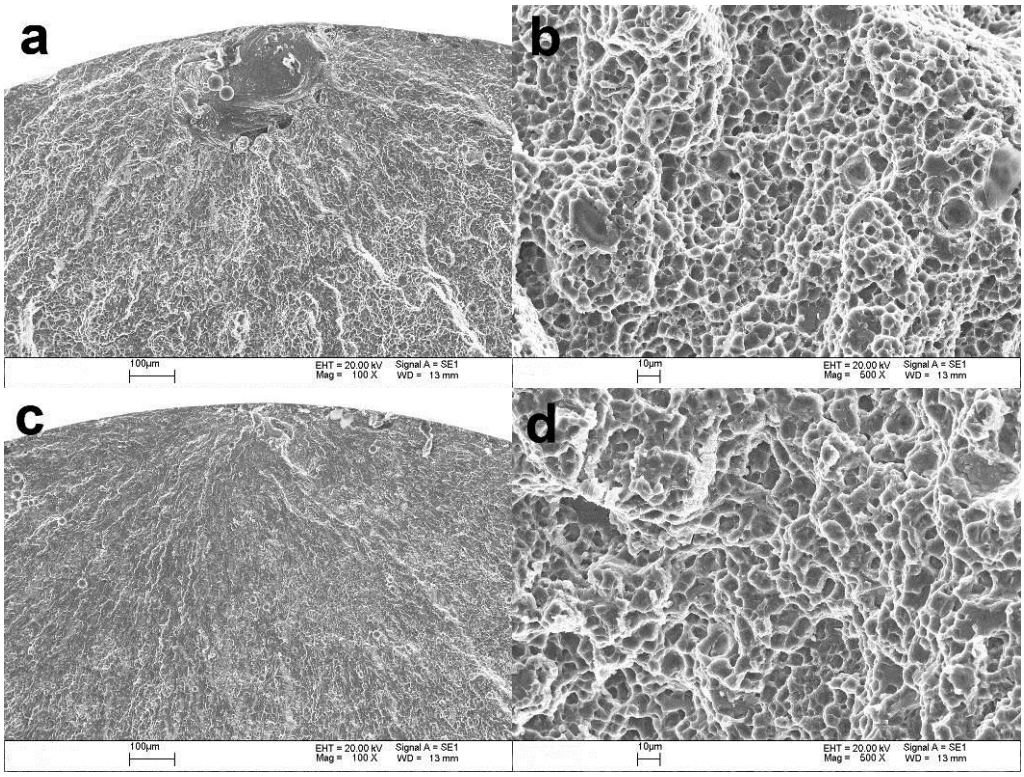

Figure 23 Typical fracture surfaces of two samples of batch #16 (300°C/90°/Peak-hardened): (a) crack initiation site and (b) area of forced fracture of sample #16.7; (c) crack initiation site and (d) area of forced fracture of sample #16.3

Tables

Table 1 Chemical composition of the alloy AlSi10Mg [13]

Al	Si	Fe	Cu	Mn	Mg	Zn	Ti
Balance	9.0-11.0	0.3	0.03	0.001-0.4	0.2-0.5	0.1	0.15

Table 2 Details of the high cycle fatigue batches

Batch number	Amount of samples	Platform temperature [°C]	Building direction [°]	Peak-hardened (T6)
#10	12	30	0	Yes
#11	10	30	90	Yes
#12	10	30	45	Yes
#13	9	300	0	No (as-built)
#14	10	300	0	Yes
#15	10	300	90	No (as-built)
#16	10	300	90	Yes
#17	10	300	45	No (as-built)
#18	10	300	45	Yes

Table 3 Design of experiments matrix (full-factorial, 2 levels, 3 factors); static tensile and high cycle fatigue properties of batches #1 and #5 are published in [18]

	Factor			Weibull constants			
	A	B	C	c_1 (45% of fatigue limit)	c_2 (45% of tensile strength)	c_3	c_4
Batch number	Platform temperature	Building direction	Post heat treatment	[MPa]	[MPa]	[1]	[1]
#1	Low (30°C)	Low (0°)	Low (as-built)	30.8	127	10.6	4.9
#10	Low (30°C)	Low (0°)	High (peak-hard.)	90.3	154.4	4.8	4.4
#5	Low (30°C)	High (90°)	Low (as-built)	61.5	159	10.5	3.6
#11	Low (30°C)	High (90°)	High (peak-hard.)	51.5	148.5	4.8	6.6
#13	High (300°C)	Low (0°)	Low (as-built)	45.5	112.5	4.7	4.7
#14	High (300°C)	Low (0°)	High (peak-hard.)	63.2	158.9	5	4.7
#15	High (300°C)	High (90°)	Low (as-built)	34.5	121.5	4.3	1.1
#16	High (300°C)	High (90°)	High (peak-hard.)	74.9	153.5	4.9	6.7

Table 4 Correlation and probability analysis of the Weibull constants $c_1 - c_4$

	c_1 (45% of fatigue limit)	c_2 (45% of tensile strength)	c_3	c_4
c_1 (45% of fatigue limit)	Correlation: 1 p = 0	Correlation: 0.747 p = 0.033 < 0.05	Correlation: -0.278 p = 0.505	Correlation: 0.344 p = 0.403
c_2 (45% of tensile strength)	Correlation: 0.747 p = 0.033 < 0.05	Correlation: 1 p = 0	Correlation: 0.082 p = 0.848	Correlation: 0.364 p = 0.375
c_3	Correlation: -0.278 p = 0.505	Correlation: 0.082 p = 0.848	Correlation: 1 p = 0	Correlation: -0.056 p = 0.896
c_4	Correlation: 0.344 p = 0.403	Correlation: 0.364 p = 0.375	Correlation: -0.056 p = 0.896	Correlation: 1 p = 0